

Instabilities near the onset of spin density wave order in metals

Max A. Metlitski and Subir Sachdev

Department of Physics, Harvard University, Cambridge MA 02138, USA

E-mail: metlitski@physics.harvard.edu, sachdev@physics.harvard.edu

Abstract. We discuss the low energy theory of two-dimensional metals near the onset of spin density wave order. It is well known that such a metal has a superconducting instability induced by the formation of spin-singlet pairs of electrons, with the pairing amplitude changing sign between regions of the Fermi surface connected by the spin density wave ordering wavevector. Here we review recent arguments that there is an additional instability which is nearly as strong: towards the onset of a modulated bond order which is locally an Ising-nematic order. This new instability is a consequence of an emergent ‘pseudospin’ symmetry of the low energy theory—the symmetry maps the sign-changing pairing amplitude to the bond order parameter.

Submitted to: *New Journal of Physics*, special issue on “*Fermiology of Cuprates*”,
edited by Mike Norman and Cyril Proust

1. Introduction

A number of recent experimental developments have refocused attention on a relatively simple picture [1, 2] of the origin of superconductivity in quasi-two-dimensional correlated electron compounds. Exchange of spin density wave (SDW) fluctuations induces an attractive interaction between electrons in a spin-singlet, even-parity channel, with the pair wavefunction changing signs between regions of the Fermi surface connected by the SDW ordering wavevector.

In the pnictide superconductors, experiments identified the nature of the SDW order and the configuration of the Fermi surface, and this theory then implies superconductivity with s_{\pm} pairing [3, 4], for which strong evidence has recently appeared [5].

In the cuprates, this picture correctly predicted the d -wave pairing signature. However, it faced the difficulty that no strong SDW fluctuations were experimentally observed in the optimal hole-doping region, where the superconductivity was the strongest. A potential resolution is offered by the theory of competing orders [6, 7, 8]. In the strong-coupling regime, the superconducting pairing amplitude has a significant feedback effect on the SDW fluctuations, and shrinks the region of long-range SDW order [9]; consequently the SDW fluctuations are also substantially reduced at low temperatures in the region of strongest superconductivity. An immediate consequence of this theory is that the SDW order should re-emerge when superconductivity is suppressed by an applied magnetic field. Such a re-emergence has been observed in a variety of experiments on both the LSCO and YBCO series of compounds [10, 11, 12, 13, 14]. The high-field quantum oscillations [15] are also naturally understood in this theory, with the re-emergent long-range SDW, or associated, order breaking up the Fermi surface into Fermi pockets.

Motivated by these developments, we recently presented [16] a detailed low energy description of the vicinity of the SDW transition in two-dimensional metals. Here we will review our main results on the additional instabilities present near such a transition. We will phrase our results for the case of the cuprate Fermi surface configuration, although there are natural extensions to the pnictides [9]. As expected [1, 17], we find an instability to spin-singlet d -wave pairing. However, the pairing instability is enhanced from the familiar BCS logarithmic divergence to a logarithm squared. We also find a dominant secondary instability to a certain modulated bond order which is locally an Ising-nematic order: this instability is also associated with a susceptibility which diverges as a logarithm squared, but with a co-efficient which is smaller than that of the pairing instability.

2. Low energy theory

We begin with a Hubbard-like model for electrons $c_{i\sigma}$ on the sites (i) of the square lattice ($\sigma = \uparrow\downarrow$ is the spin index) with dispersion $\varepsilon_{\vec{k}}$ as a function of wavevector \vec{k} . We

decouple the repulsive interaction in the spin channel by a Hubbard-Stratonovich field ϕ^a ($a = x, y, z$). This bosonic field ϕ^a represents collinear SDW order at wavevector $\vec{Q} = (\pi, \pi)$. In this manner we obtain the familiar “spin-fermion” model for the vicinity of the SDW ordering transition [1, 17] with the Lagrangian

$$\begin{aligned} \mathcal{L} = & \int_{\vec{k}} c_{\vec{k}\sigma}^\dagger \left(\frac{\partial}{\partial \tau} + \varepsilon_{\vec{k}} \right) c_{\vec{k}\sigma} - \lambda \sum_i \phi_i^a c_{i\sigma}^\dagger \tau_{\sigma\sigma'}^a c_{i\sigma'} e^{i\vec{Q}\cdot\vec{r}_i} \\ & + \int d^2x \left[\frac{1}{2c^2} (\partial_\tau \phi^a)^2 + \frac{1}{2} (\nabla_x \phi^a)^2 + \frac{r}{2} (\phi^a)^2 + \frac{u}{4} ((\phi^a)^2)^2 \right] \end{aligned} \quad (1)$$

Here τ is imaginary time, τ^a are the Pauli matrices, and we have partially integrated out high energy electrons to generate a bare ϕ^4 field theory Lagrangian for the SDW order parameter. The couplings r and u tune the strength of the SDW fluctuations: in mean-field theory there is an onset of long-range SDW order at $r = 0$.

The Lagrangian in (1) is not yet in the form of a low energy theory amenable to a continuum renormalization group (RG) analysis. This is because of the transfer with the large wavevector \vec{Q} in the spin-fermion term λ : this will scatter fermions with momenta well away from the Fermi surface, and so involves high energy excitations.

We focus on the low energy sector by zeroing in on the “hot spots”. These are special locations on the Fermi surface where $\varepsilon_{\vec{k}+\vec{Q}} = \varepsilon_{\vec{k}}$: for these points, both the initial and final electron states in the spin-fermion coupling can be right on the Fermi surface, and so the scattering from the SDW fluctuations is the strongest. For the electron dispersion appropriate to the cuprates, there are $n = 4$ pairs of hot spots, as shown in Fig. 1. We introduce fermion fields $(\psi_{1\sigma}^\ell, \psi_{2\sigma}^\ell)$, $\ell = 1 \dots n$, $\sigma = \uparrow \downarrow$ for each pair of hot spots. Lattice rotations map the pairs of hot spots into each other, acting cyclically on the index ℓ . Moreover, the two hot spots within each pair are related by a reflection across a lattice diagonal. It will be useful to promote each field ψ to have N -flavors with an eye to performing a $1/N$ expansion. (Note that in Ref. [17], the total number of hot spots $2nN$ is denoted as N .) The flavor index is suppressed in all the expressions. The low energy effective theory is then given by the following Lagrangian density in 2+1 spacetime dimensions for the boson ϕ^a and the fermions ψ

$$\begin{aligned} L = & \frac{N}{2c^2} (\partial_\tau \phi^a)^2 + \frac{N}{2} (\nabla_x \phi^a)^2 + \frac{Nr}{2} (\phi^a)^2 + \frac{Nu}{4} ((\phi^a)^2)^2 \\ & + \psi_1^{\ell\dagger} (\partial_\tau - i\vec{v}_1^\ell \cdot \nabla_x) \psi_1^\ell + \psi_2^{\ell\dagger} (\partial_\tau - i\vec{v}_2^\ell \cdot \nabla_x) \psi_2^\ell \\ & + \lambda \phi^a \left(\psi_{1\sigma}^{\ell\dagger} \tau_{\sigma\sigma'}^a \psi_{2\sigma'}^\ell + \psi_{2\sigma}^{\ell\dagger} \tau_{\sigma\sigma'}^a \psi_{1\sigma'}^\ell \right). \end{aligned} \quad (2)$$

The first line in Eq. (2) is the usual O(3) model for the SDW order parameter, the second line is the fermion kinetic energy, and the third line is the interaction between the SDW order parameter and the fermions at the hot spots. Here, we have linearized the fermion dispersion near the hot spots, and \vec{v}^ℓ are the corresponding Fermi velocities. It is convenient to choose coordinate axes along directions $\hat{x} = \frac{1}{\sqrt{2}}(1, 1)$ and $\hat{y} = \frac{1}{\sqrt{2}}(-1, 1)$, so that

$$\vec{v}_1^{\ell=1} = (v_x, v_y) \quad , \quad \vec{v}_2^{\ell=1} = (-v_x, v_y), \quad (3)$$

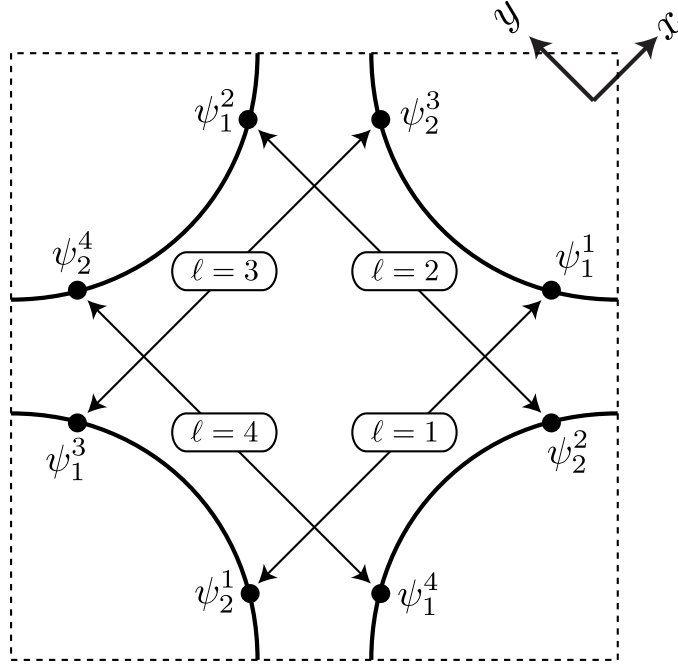


Figure 1. Square lattice Brillouin zone showing the Fermi surface appropriate to the cuprates. The filled circles are the hot spots connected by the SDW wavevector $\vec{Q} = (\pi, \pi)$. The locations of the continuum fermion fields ψ_1^ℓ and ψ_2^ℓ are indicated.

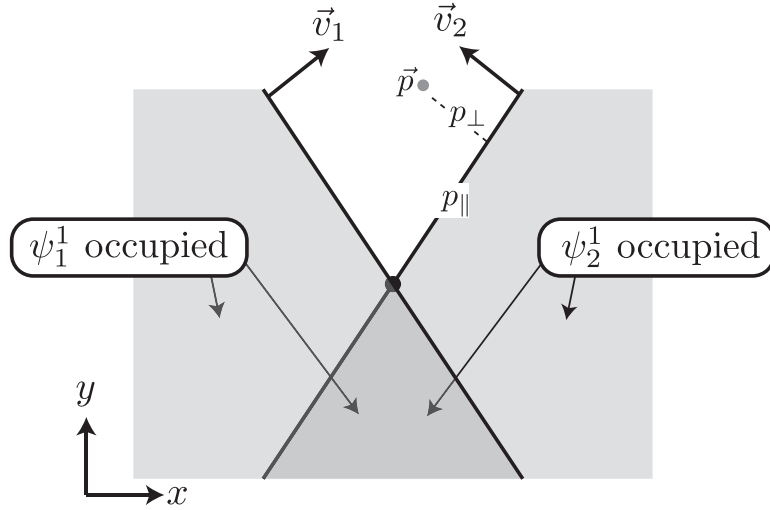


Figure 2. Configuration of the $\ell = 1$ pair of hot spots, with the momenta of the fermion fields measured from the common hot spot at $\vec{k} = 0$, indicated by the dark filled circle. The Fermi velocities $\vec{v}_{1,2}$ of the $\psi_{1,2}$ fermions are indicated. The momentum components of the $\psi_2^1(\vec{p})$ fermion parallel (p_{\parallel}) and orthogonal (p_{\perp}) to the Fermi surface are indicated.

The velocity ratio $\alpha = v_y/v_x$ plays an important role in the RG analysis of (2). The Fermi velocities (3) are indicated in Fig. 2. The other Fermi velocities are related by rotations, $\vec{v}^\ell = (R_{\pi/2})^{\ell-1}\vec{v}^{\ell=1}$.

3. Pseudospin symmetry

We now note a crucial symmetry of the theory (2), which will be important for the instabilities discussed in this paper. Besides the microscopic translation, point-group, spin-rotation and time-reversal symmetries, the low energy theory possesses a set of four emergent SU(2) pseudospin symmetries associated with particle-hole transformations. Let us introduce a four-component spinor,

$$\Psi_i^\ell = \begin{pmatrix} \psi_i^\ell \\ i\tau^2 \psi_i^{\ell\dagger} \end{pmatrix} \quad (4)$$

We will denote the particle-hole indices in the four-component spinor by α, β . The spinor (4) satisfies the hermiticity condition,

$$i\tau^2 \begin{pmatrix} 0 & -1 \\ 1 & 0 \end{pmatrix} \Psi_i^\ell = \Psi_i^{\ell*} \quad (5)$$

Then, the fermion part of the Lagrangian (2) can be rewritten as,

$$L_\psi = \frac{1}{2} \Psi_1^{\ell\dagger} (\partial_\tau - i\vec{v}_1^\ell \cdot \nabla) \Psi_1^\ell + \frac{1}{2} \Psi_2^{\ell\dagger} (\partial_\tau - i\vec{v}_2^\ell \cdot \nabla) \Psi_2^\ell + \frac{1}{2} \lambda \phi^a \cdot \left(\Psi_1^{\ell\dagger} \tau^a \Psi_2^\ell + \Psi_2^{\ell\dagger} \tau^a \Psi_1^\ell \right). \quad (6)$$

Now the Lagrangian (6) and the condition (5) are manifestly invariant under,

$$\text{SU}(2)_\ell : \Psi_i^\ell \rightarrow U_\ell \Psi_i^\ell \quad , \quad \phi^a \rightarrow \phi^a \quad (7)$$

where the U_ℓ are SU(2) matrices. Note that there are 4 independent SU(2) pseudospin symmetries, one for each pair of hot spots. The diagonal subgroup of (7) is associated with independent conservation of the fermion number at each hot spot pair.

The symmetry (7) is a consequence of linearization of the fermion spectrum near the hot spots and is broken by higher order terms in the dispersion. The diagonal subgroup noted above is preserved by higher order terms in the dispersion, but is broken by four-fermion interactions, which map fermion pairs from opposite hot spots into each other. Both symmetry breaking effects are irrelevant [16] in the low energy limit used to derive (2).

This large quadrupled SU(2) symmetry is thus a generic feature of the vicinity of the SDW ordering transition in metals. It should be contrasted with the more familiar lattice SU(2) pseudospin symmetry of the Hubbard model [18, 19]: there is only a single such SU(2) symmetry, present at half-filling, and only if the dispersion has a particle-hole symmetric form *i.e.* the electron hopping is always between opposite sublattices. No such restrictions are placed in our case. We will also find a connection between instabilities in the particle-hole and particle-particle channels, but both will apply to the generic spin-fermion model in (2).

The pseudospin symmetry (7) constrains the form of the fermion Green's function to be,

$$- \langle \Psi_{i\alpha\sigma}^\ell \Psi_{j\beta\sigma'}^{m\dagger} \rangle = \delta^{\ell m} \delta_{ij} \delta_{\alpha\beta} \delta_{\sigma\sigma'} G_i^\ell(x - x') \quad (8)$$

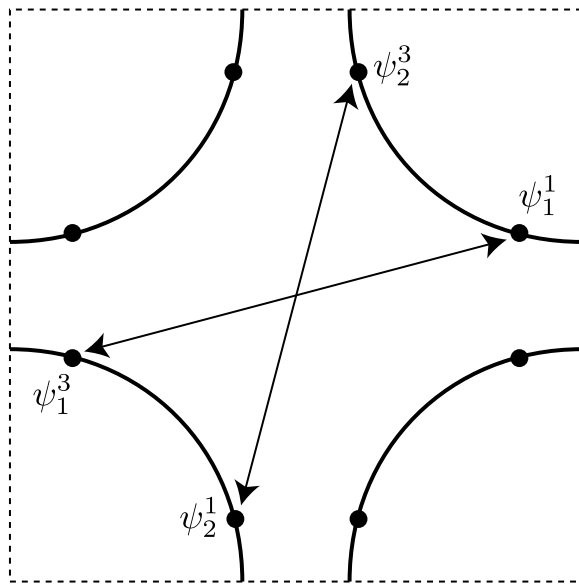


Figure 3. Pairing of the electrons at the $\ell = 1, 3$ hot spots of Fig. 1. Electrons at opposite ends of the arrows form spin-singlet pairs. The pairing amplitude is in the spin-singlet channel and has opposite signs on the two arrows. There is a similar pairing instability between the $\ell = 2, 4$ hot spots.

which implies,

$$G_i^\ell(x - x') = -G_i^\ell(x' - x) \quad (9)$$

The corresponding expression in momentum space, $G_i^\ell(k) = -G_i^\ell(-k)$, implies that the location of hot spots in the Brillouin zone is not renormalized by the spin wave fluctuations in the low energy theory.

4. Pairing instability

A detailed RG analysis of the SDW transition described by (2) was presented in Ref. [16] using the framework of the $1/N$ expansion. We will not describe this here, but will use a few key results below.

Let us directly proceed to discuss the nature of the pairing instability. The pairing is induced by ϕ -fluctuations, which play the role of the phonon mode in conventional BCS theory. The pairing involves 2 pairs of hot spots, consisting of time-reversed pairs of electrons, as shown in Fig. 3. The spin singlet superconducting order parameter, associated with Fig. 3 is

$$C = \epsilon_{\sigma\sigma'} (\psi_{1\sigma}^{1\dagger} \psi_{1\sigma'}^{3\dagger} - \psi_{2\sigma}^{1\dagger} \psi_{2\sigma'}^{3\dagger}) \quad (10)$$

and the relative sign between the two terms is the signature of d -wave pairing. Thus, the operator (10) is odd under a reflection about the lattice diagonal $P : (k_x, k_y) \rightarrow (-k_x, k_y)$.

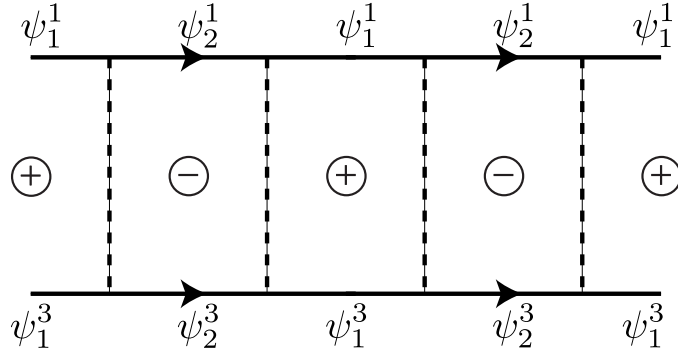


Figure 4. Cooperon diagram associated with the pairing instability of the $\ell = 1, 3$ hot spots. The full lines are the fermion propagators, as indicated, and the dashed line is the propagator of the SDW fluctuation ϕ^a . The circled signs indicate the signs of the pairing amplitude of the corresponding pairs of fermions.

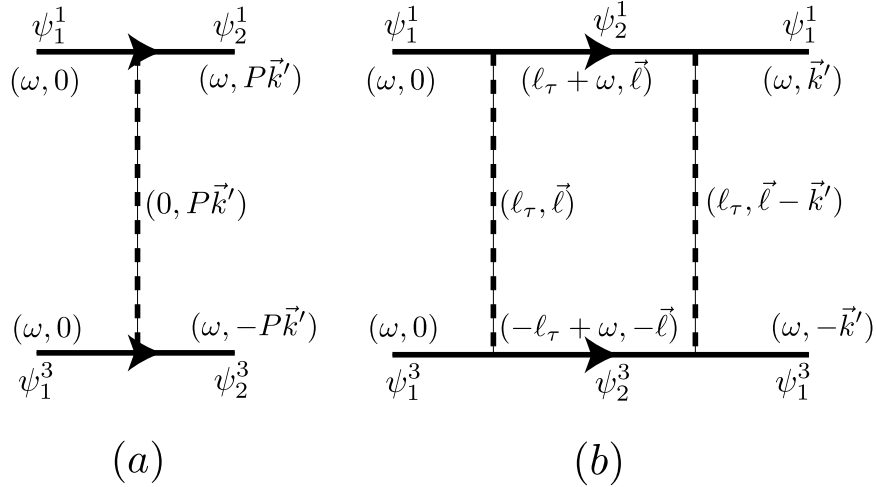


Figure 5. The first two terms in the ladder series of Fig. 4, with frequency/momentum labels, as evaluated in Eqs. (13) and (14).

The pairing instability in the channel (10) is described by computing the four-fermion scattering amplitude,

$$\begin{aligned} \Gamma_{\text{BCS}}(\vec{k}, \omega_1, -\vec{k}, \omega_3; \vec{k}', \omega'_1, -\vec{k}', \omega'_3) = & \\ \epsilon_{\sigma\sigma'}\epsilon_{\rho\rho'} \left\langle \left(\psi_{1\sigma}^1(\vec{k}', \omega'_1)\psi_{1\sigma'}^3(-\vec{k}', \omega'_3) - \psi_{2\sigma}^1(P\vec{k}', \omega'_1)\psi_{2\sigma'}^3(-P\vec{k}', \omega'_3) \right) \right. & \\ \left. \times \left(\psi_{1\rho'}^{3\dagger}(-\vec{k}, \omega_3)\psi_{1\rho}^{1\dagger}(\vec{k}, \omega_1) - \psi_{2\rho'}^{3\dagger}(-P\vec{k}, \omega_3)\psi_{2\rho}^{1\dagger}(P\vec{k}, \omega_1) \right) \right\rangle, & \quad (11) \end{aligned}$$

where it is understood that the external fermion Green's functions have been truncated. As in conventional BCS theory, we will study the contribution of the Cooperon ladder diagrams illustrated in Fig. 4 to the amplitude (11). Here we will only examine the first two terms in the series, as shown in Fig. 5. The dashed line denotes the propagator of the ϕ field, representing the SDW fluctuations. For this we use the overdamped

paramagnon form appropriate to the $1/N$ expansion,

$$D(\omega, \vec{q}) = \frac{1}{N} \frac{1}{(\gamma|\omega| + \vec{q}^2)}, \quad (12)$$

where $\gamma = n\lambda^2/(2\pi v_x v_y)$ is the damping constant obtained from a decay of a $\vec{\phi}$ into a particle-hole pair.

The strongest infra-red enhancement of the scattering amplitude by SDW fluctuations occurs in the kinematic regime when the incoming fermions have momenta at hot spots $\vec{k} = 0$, while the outgoing fermions are “cold”, *i.e.* their momentum \vec{k}' is along the Fermi surface and their frequency satisfies $\gamma|\omega| \ll \vec{k}'^2$. For simplicity, we set all the external frequencies to be equal $\omega_1 = \omega_3 = \omega'_1 = \omega'_3 = \omega$. With the above choice of external momenta the diagram in Fig. 5a evaluates to

$$\Gamma_{\text{BCS}}^{\text{tree}} = \frac{12\lambda^2}{N\gamma|\vec{k}'|^2} \quad (13)$$

Next, we consider the diagram for the BCS amplitude in Fig. 5b, which evaluates to

$$\Gamma_{\text{BCS}}^{\text{1loop}} = 36\lambda^4 \int \frac{d\ell_\tau d^2\vec{\ell}}{(2\pi)^3} D(\ell_\tau, \vec{\ell}) G_2^1(\ell_\tau + \omega, \vec{\ell}) G_2^3(-\ell_\tau + \omega, -\vec{\ell}) D(\ell_\tau, \vec{\ell} - \vec{k}') \quad (14)$$

where G denotes the fermion Green’s function. The main contribution to Eq. (14) comes from momenta $|\vec{\ell}| \ll |\vec{k}'|$, $\gamma|\ell_\tau| \ll \vec{k}'^2$ such that the first scattering in Fig. 5b is “soft”, while the second one is “hard”. Then,

$$\Gamma_{\text{BCS}}^{\text{1loop}} \approx \frac{36\lambda^4}{N\gamma|\vec{k}'^2|} \int \frac{d\ell_\tau d^2\vec{\ell}}{(2\pi)^3} D(\ell_\tau, \vec{\ell}) G_2^1(\ell_\tau + \omega, \vec{\ell}) G_2^3(-\ell_\tau + \omega, -\vec{\ell}) \quad (15)$$

Now we need the form of G near the SDW critical point. This was described in some detail in Ref. [16] to one-loop order in the $1/N$ expansion: it has a complex structure depending upon the value of frequency and momentum from the hot spot. For the BCS scattering amplitude, it turns out [16] that the dominant contribution comes from the Fermi liquid poles on the “cold lines” in the vicinity of the hot spot. Let us define p_\perp as the distance to the Fermi surface, and p_\parallel as the distance to the hot spot (see Fig. 2); then there are well-defined Landau quasiparticles for $p_\perp \ll p_\parallel$ and $\gamma|\omega| \ll p_\parallel^2$, with

$$G(\omega, \vec{p}) \sim \frac{\mathcal{Z}(p_\parallel)}{i\omega - v_F(p_\parallel)p_\perp}. \quad (16)$$

The Fermi velocity v_F and the quasiparticle residue \mathcal{Z} both vanish linearly with p_\parallel as we approach the hot spot [16],

$$v_F(p_\parallel) = \frac{4nN}{3\gamma\lambda^2} p_\parallel, \quad \mathcal{Z}(p_\parallel) = \frac{4N}{3\lambda^2} (2\pi n)^{1/2} \gamma^{-1/2} \left(\frac{1}{\alpha} + \alpha \right)^{-1/2} p_\parallel, \quad (17)$$

where recall $\alpha = v_y/v_x$. We now insert (12), (16), and (17) into (15) and obtain

$$\Gamma_{\text{BCS}}^{\text{1loop}} = - \frac{36\lambda^4}{N^2\gamma|\vec{k}'^2|} \int \frac{d\ell_\parallel}{2\pi} \int \frac{d\ell_\tau}{2\pi} \int \frac{d\ell_\perp}{2\pi} \frac{1}{(\gamma|\ell_\tau| + \ell_\parallel^2)}$$

$$\times \frac{\mathcal{Z}(\ell_{\parallel})}{[i(\ell_{\tau} + \omega) - v_F(\ell_{\parallel})\ell_{\perp}]} \frac{\mathcal{Z}(\ell_{\parallel})}{[i(\ell_{\tau} - \omega) + v_F(\ell_{\parallel})\ell_{\perp}]}, \quad (18)$$

where $\ell_{\parallel, \perp}$ are defined with respect to the $\psi_2^{1,3}$ Fermi surfaces, as in Fig. 2. Recalling that the internal fermions are taken to be cold, *i.e.* $\gamma|\ell_{\tau}| \ll \ell_{\parallel}^2$, we may approximate the bosonic propagator in Eq. (18) by its static value. After changing variables to $\epsilon = v_F(\ell_{\parallel})\ell_{\perp}$ we then obtain,

$$\Gamma_{\text{BCS}}^{\text{1loop}} = -\frac{36\lambda^4}{N^2\gamma|\vec{k}'^2|} \int \frac{d\ell_{\parallel}}{2\pi} \frac{\mathcal{Z}^2(\ell_{\parallel})}{v_F(\ell_{\parallel})\ell_{\parallel}^2} \times \int_{\gamma|\ell_{\tau}| \lesssim \ell_{\parallel}^2} \frac{d\ell_{\tau}}{2\pi} \int \frac{d\epsilon}{2\pi} \frac{1}{[i(\ell_{\tau} + \omega) - \epsilon]} \frac{1}{[i(\ell_{\tau} - \omega) + \epsilon]}. \quad (19)$$

The integral over ℓ_{τ} , ϵ has the form familiar from Fermi-liquid theory and gives the usual BCS logarithm,

$$\int \frac{d\ell_{\tau}}{2\pi} \int \frac{d\epsilon}{2\pi} \frac{1}{[i(\ell_{\tau} + \omega) - \epsilon]} \frac{1}{[i(\ell_{\tau} - \omega) + \epsilon]} = -\frac{1}{2\pi} \log \frac{\Lambda_{FL}}{|\omega|} \quad (20)$$

where Λ_{FL} is the frequency/energy cut-off, which in the present case is $\Lambda_{FL} \sim \ell_{\parallel}^2/\gamma$. Of course, for the above form to hold, we need $|\omega| \ll \Lambda_{FL}$. Thus,

$$\begin{aligned} \Gamma_{\text{BCS}}^{\text{1loop}} &= \left(\frac{12\lambda^2}{N\gamma|\vec{k}'^2|} \right) \frac{3\lambda^2}{2\pi^2 N} \int_{\sqrt{\gamma\omega}}^{|\vec{k}'|} d\ell_{\parallel} \frac{\mathcal{Z}^2(\ell_{\parallel})}{v_F(\ell_{\parallel})\ell_{\parallel}^2} \log \frac{\ell_{\parallel}^2}{\gamma|\omega|} \\ &= \left(\frac{12\lambda^2}{N\gamma|\vec{k}'^2|} \right) \frac{\alpha}{\pi(\alpha^2 + 1)} \log^2 \frac{\vec{k}'^2}{\gamma|\omega|} \end{aligned} \quad (21)$$

where we have cut-off the ultra-violet divergence of the ℓ_{\parallel} integral by $|\vec{k}'|$. Comparing Eq. (21) with Eq. (13) we see that there is an enhancement of the Cooperon propagator by the factor

$$1 + \frac{\alpha}{\pi(\alpha^2 + 1)} \log^2 \frac{\vec{k}'^2}{\gamma|\omega|} \quad (22)$$

which has the promised log-squared form. Note that this is not suppressed by a factor of $1/N$. As we noted, the critical SDW fluctuations enhance the BCS logarithm to the stronger divergence above. Note that this divergence came from “cold” internal fermion lines in Fig. 5b; thus, similar effects will also be present in higher order graphs in the Cooperon ladder.

It is not clear how to improve Eq. (22) using the RG. However, we can note that the coupling α is of order unity, and so the pairing is enhanced as the frequency crosses the Fermi energy. We also note that in the two-loop RG, the coupling $\alpha = v_y/v_x$ has a flow towards weak coupling

$$\frac{d\alpha}{d\ell} = -\frac{12}{\pi n N} \frac{\alpha^2}{(1 + \alpha^2)}$$

but it not appropriate to simply insert the integrated value from this flow into the pairing enhancement.

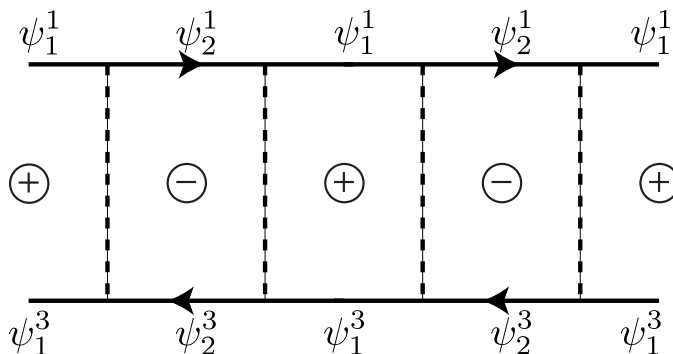


Figure 6. Pseudospin partner of the Cooperon susceptibility in Fig 4, obtained by reversing the line of the $\ell = 3$ fermion. As described in the text, this represents the susceptibility to a modulated bond order which is locally an Ising-nematic order.

5. Bond order instability

Let us now apply the pseudospin transformation in (7) to *only* the $\ell = 3$ pair of hot spots, while leaving the $\ell = 1$ pair unchanged. This will transform the Cooperon instability in the particle-particle channel to an instability in the particle-hole channel. Diagrammatically, this corresponds to reversing the $\ell = 3$ line in Fig. 4 to obtain the susceptibility in Fig. 6. By the symmetry of the low energy theory in Section 3, it would seem we can immediately conclude that the scattering amplitude in Fig. 6 should also have a log-squared divergence at one loop order as in (21). However, as was shown in [16], the naively irrelevant curvature of the Fermi surface, which breaks the pseudospin symmetry, modifies the result in the particle-hole channel at very low frequencies $|\omega| \ll A|\vec{k}'|^3$, where A is a co-efficient related to the curvature. It was found that in this regime, the log-squared divergence did indeed survive, but with a co-efficient which was smaller by a factor of 3. Thus in place of the factor in Eq. (22) for Fig. 4, the amplitude in Fig. 6 has the enhancement factor

$$1 + \frac{\alpha}{3\pi(\alpha^2 + 1)} \log^2 \frac{\vec{k}'^2}{\gamma|\omega|}. \quad (23)$$

Moreover, for higher frequencies, $\omega \gg A|\vec{k}'|^3$, the particle-particle and particle-hole channels are degenerate.

What type of ordering does the susceptibility in Fig. 6 correspond to? We can deduce this by performing the pseudospin transformation on Fig. 3: this changes the $\ell = 3$ fermions from particles to holes, leading to Fig. 7. Using Eq. (10), this makes it clear that the scattering amplitude in Fig. 6 is that associated with the ordering of the operator

$$O = \left(\psi_{1\sigma}^{1\dagger} \psi_{1\sigma}^3 - \psi_{2\sigma}^{1\dagger} \psi_{2\sigma}^3 \right), \quad (24)$$

and the sign between the two terms is the pseudospin descendant of the d -wave pairing. Unlike, the Cooper pair operator, the operator O carries a non-zero momentum \vec{Q}_1 , as

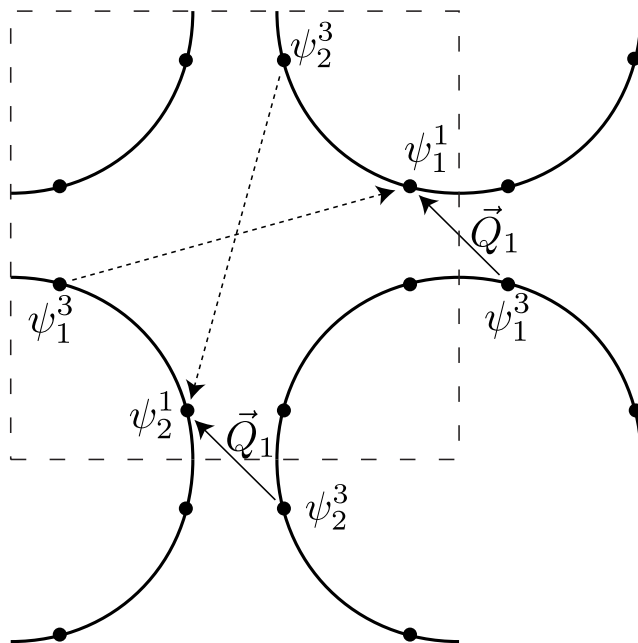


Figure 7. Spin singlet density operators ($\sim \psi^\dagger\psi$) of the electrons at the $\ell = 1, 3$ hot spots of Fig. 1 shown with an arrow pointing from the Brillouin zone location of ψ to that of ψ^\dagger . The dashed arrows are the density operators in the first Brillouin zone. The full arrows are in an extended zone scheme which shows that these operators have net momentum $\vec{Q}_1 = 2K_y(-1, 1)$, where (K_x, K_y) is the location of the $\ell = 1, i = 1$ hot spot (we have $K_x + K_y = \pi$). The density operator with opposite signs on the two arrows is enhanced near the SDW critical point. Similarly the $\ell = 2, 4$ hot spots contribute density operators at $\vec{Q}_2 = 2K_y(1, 1)$.

shown in Fig. 7. For the cuprate Fermi surface, this is a small momentum oriented along a square lattice diagonal. This non-zero momentum would suggest that O is a charge density wave at wavevector \vec{Q}_1 . However, this does not account for the relative sign in (24), which implies that O changes sign upon reflection about the square lattice diagonal parallel to \vec{Q}_1 . The situation becomes clearer, when we write (24) in terms of the underlying lattice fermions $c_{\vec{k}\sigma}$. The state in which $\langle O \rangle \neq 0$ has

$$\left\langle c_{\vec{k}-\vec{Q}_1/2,\sigma}^\dagger c_{\vec{k}+\vec{Q}_1/2,\sigma} \right\rangle \sim (\cos k_x - \cos k_y) \quad (25)$$

Despite the d -wave-like structure, this order is *not* the popular d -density wave [20]; the latter is odd under time-reversal, and in the present notation takes the form

$$\left\langle c_{\vec{k}-\vec{Q}/2,\sigma}^\dagger c_{\vec{k}+\vec{Q}/2,\sigma} \right\rangle \sim i(\sin k_x - \sin k_y), \quad (26)$$

with $\vec{Q} = (\pi, \pi)$. The order in (26) is not enhanced near the SDW critical point, while that in (25) is. By taking the Fourier transform of (25), it is easy to see that O does not lead to any modulations in the site charge density $\langle c_{\vec{r}\sigma}^\dagger c_{\vec{r}\sigma} \rangle$, and so it is not a charge density wave. The non-zero modulations occur in the off-site correlations $\langle c_{\vec{r}\sigma}^\dagger c_{\vec{s}\sigma} \rangle$ with

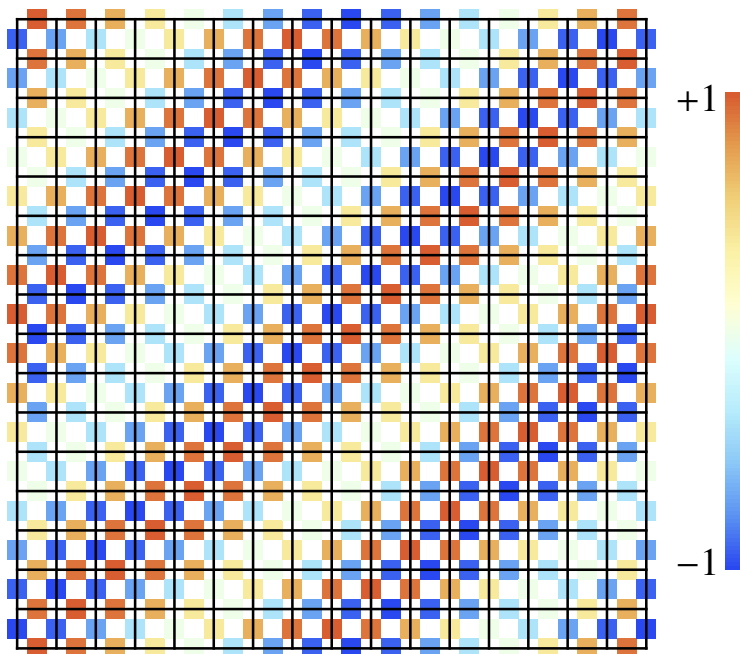


Figure 8. Plot of the bond density modulations in (27). The lines are the links of the underlying square lattice. Each link contains a colored square representing the value of $\langle c_{\vec{r}\sigma}^\dagger c_{\vec{s}\sigma} \rangle$, where \vec{r} and \vec{s} are the sites at the ends of the link. We chose the ordering wavevector $\vec{Q}_1 = (2\pi/16)(1, -1)$. Notice the local Ising-nematic ordering, and the longer wavelength sinusoidal envelope along the diagonal.

$\vec{r} \neq \vec{s}$. For \vec{r} and \vec{s} nearest-neighbors, we have

$$\langle c_{\vec{r}\sigma}^\dagger c_{\vec{s}\sigma} \rangle \sim \left(\langle O \rangle e^{i\vec{Q}_1 \cdot (\vec{r} + \vec{s})/2} + \text{c.c.} \right) [\delta_{\vec{r}-\vec{s}, \hat{x}} + \delta_{\vec{s}-\vec{r}, \hat{x}} - \delta_{\vec{r}-\vec{s}, \hat{y}} - \delta_{\vec{s}-\vec{r}, \hat{y}}], \quad (27)$$

where \hat{x} and \hat{y} are unit vectors corresponding to the sides of the square lattice unit cell. The modulations in the nearest neighbor bond variables $\langle c_{\vec{r}\sigma}^\dagger c_{\vec{r}+\hat{x}, \sigma} \rangle$ and $\langle c_{\vec{r}\sigma}^\dagger c_{\vec{r}+\hat{y}, \sigma} \rangle$ are plotted in Figs. 8 and 9. These observables measure spin-singlet correlations across a link: if there are 2 electrons on the 2 sites of a link, this observable takes different values depending upon whether the electrons are in a spin singlet or a spin triplet state. Thus O has the local character of a valence bond solid (VBS) order parameter. The first factor on the rhs of Eq. (27) shows that the VBS order has modulations at the wavevector \vec{Q}_1 along a square lattice diagonal. As we saw in Fig. 7, $|\vec{Q}_1|$ is small and so the first factor in (27) contributes a relatively long-wavelength modulation, as is evident from Figs. 8 and 9. This long-wavelength modulation serves as an envelope to the oscillations given by the second factor in (27). The latter indicates that the bond order has opposite signs on the x and y directed bonds: this short distance behavior corresponds locally to an *Ising-nematic* order, which is also evident in Figs. 8 and 9. The ordering in (27) becomes global Ising-nematic order in the limit $\vec{Q}_1 \rightarrow 0$. It is interesting and significant that a $\vec{Q}_1 = 0$ Ising-nematic instability appears in numerical weak-coupling renormalization group analyses [21, 22].

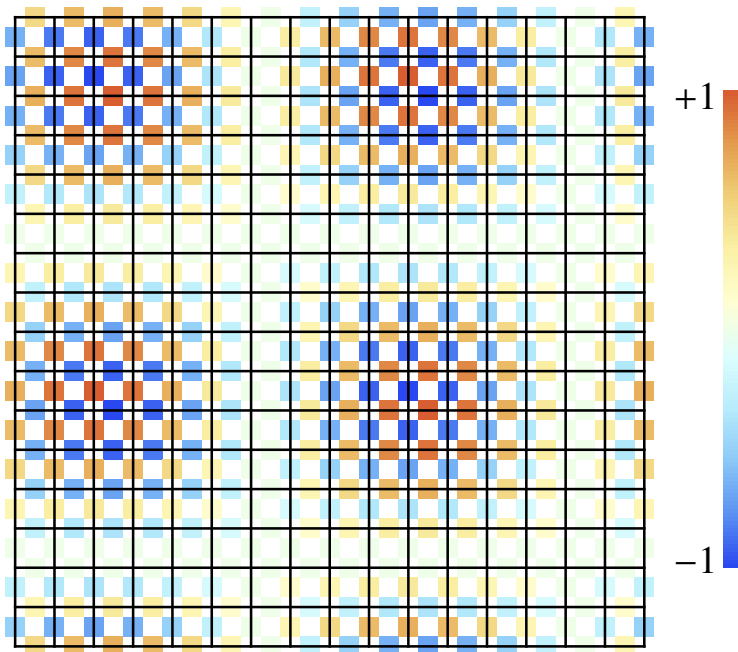


Figure 9. As in Fig. 8, but for orderings along both $\vec{Q}_1 = (2\pi/16)(1, -1)$ and $\vec{Q}_2 = (2\pi/16)(1, 1)$.

6. Conclusions

The ordering found in Section 5 has not (yet) been directly detected in any experiments on the cuprates. However, it does have a natural connection to a variety of recent experiments [23, 24, 25, 26, 27]. The ordering is present only in bond observables (see Figs. 8 and 9), and so relates to the bond-centered modulations seen in scanning tunnelling microscopy. Also, we have so far performed only a linear stability analysis near the SDW critical point. After accounting for non-linearities, and the interplay with the superconducting order parameter, generically \vec{Q}_1 will move away from the value determined by the location of the hot spots: there is no symmetry which pins the value of \vec{Q}_1 . In general, non-linearities prefer commensurate wavevectors, and so a shift to $\vec{Q}_1 = 0$ is not unreasonable. In that case, as we noted above, global Ising nematic order would appear.

Applying a magnetic field will strongly suppress the instability to d -wave superconductivity noted in Section 4. However, the particle-hole instability of Section 5 occurs in the zero charge channel, and so should be insensitive to the applied field. Thus it is possible that the ordering in (25) becomes the dominant instability at large magnetic fields, and so plays a role in the structure of the Fermi surface and the quantum oscillations.

Acknowledgements

This research was supported by the National Science Foundation under grant DMR-0757145, by the FQXi foundation, and by a MURI grant from AFOSR.

References

- [1] Scalapino D J, Loh E and Hirsch J E 1986 *Phys. Rev. B* **34**, 8190.
- [2] Scalapino D J 2010 A common thread *Preprint* arXiv:1002.2413
- [3] Mazin I I, Singh D J, Johannes M D and Du M -H 2008 *Phys. Rev. Lett.* **101**, 057003.
- [4] Seo Kangjun, Bernevig B A and Hu Jiangping 2008 *Phys. Rev. Lett.* **101**, 206404.
- [5] Hanaguri T, Niitaka S, Kuroki K and Takagi H 2010 *Science* **328**, 474.
- [6] Sachdev S and Zhang S-C 2002 *Science* **295**, 452.
- [7] Demler E, Sachdev S and Zhang Y 2001 *Phys. Rev. Lett.* **87**, 067202.
- [8] Sachdev S 2010 *Physica Status Solidi B* **247**, 537 (*Preprint* arXiv:0907.0008)
- [9] Moon E-G and Sachdev S 2010 Quantum critical point shifts under superconductivity: the pnictides and the cuprates *Preprint* arXiv:1005.3312.
- [10] Lake B *et al* 2002 *Nature* **415**, 299.
- [11] Khaykovich B, Wakimoto S, Birgeneau R J, Kastner M A, Lee Y S, Smeibidl P, Vorderwisch P and Yamada K 2005 *Phys. Rev. B* **71**, 220508.
- [12] Chang J *et al* 2008 *Phys. Rev. B* **78**, 104525.
- [13] Chang J *et al* 2009 *Phys. Rev. Lett.* **102**, 177006.
- [14] Haug D *et al* 2009 *Phys. Rev. Lett.* **103**, 017001.
- [15] Doiron-Leyraud N, Proust C, LeBoeuf D, Levallois J, Bonnemaision J-B, Liang R, Bonn D A, Hardy W N and Taillefer L 2007 *Nature* **447**, 565.
- [16] Metlitski M and Sachdev S 2010 *Phys. Rev. B* **82**, 075128.
- [17] Abanov Ar, Chubukov A V and Schmalian J 2003 *Advances in Physics* **52**, 119.
- [18] Yang C N 1989 *Phys. Rev. Lett.* **63**, 2144.
- [19] Kee H-Y 2010 *Annals of Physics* **325**, 1260.
- [20] Chakravarty S, Laughlin R B, Morr D K and Nayak C 2001 *Phys. Rev. B* **63**, 094503.
- [21] Halboth C J and Metzner W 2000 *Phys. Rev. Lett.* **85**, 5162.
- [22] Yamase H and Kohno H 2000 *J. Phys. Soc. Jpn.* **69**, 2151.
- [23] Ando Y, Segawa K, Komiya S and Lavrov A N 2002 *Phys. Rev. Lett.* **88**, 137005.
- [24] Kohsaka Y *et al* 2007 *Science* **315**, 1380.
- [25] Hinkov V, Haug D, Fauqué B, Bourges P, Sidis Y, Ivanov A, Bernhard C, Lin C T and Keimer B 2008 *Science* **319**, 597.
- [26] Daou R *et al* 2010 *Nature* **463**, 519.
- [27] Lawler M J *et al* 2010 *Nature* **466**, 347.